Real-Time *In Situ* Monitoring of the Thermal Cure of a Bisphenol Cyanate: A View Toward Intelligent Processing

JOHN B. COOPER,[1,]* THOMAS M. VESS,[1] LORI A. CAMPBELL,[1] and BRIAN J. JENSEN[2]

[1]Department of Chemistry and Biochemistry, Old Dominion University, Norfolk, Virginia 23529, and
[2]NASA Langley Research Center, Hampton, Virginia 23681

SYNOPSIS

A dispersive fiber-optic Raman spectrometer was used to remotely monitor, in real-time, the local temperature and the extent of reaction of a commercial cyanate ester polymer (AroCy L-10). The local temperature was determined by solving the Boltzmann relation governing the intensity ratio of the Raman Stokes and anti-Stokes scattering of a reference mode which does not vary with the reaction chemistry. The extent of the reaction can be monitored using either individual peaks associated with the reactant or product or by using the entire spectrum and principal component multivariate calibration. The use of principal component analysis has distinct advantages over the single-peak method. © 1996 John Wiley & Sons, Inc.

INTRODUCTION

The commercial use of high-performance thermoset polymers has accelerated in recent years due to an increasing number of demanding aerospace, automotive, and electronic applications which require several of the unique properties of these materials. Traditionally, the desired properties of a final material for a particular application were determined primarily by the selection of the reactant itself. For example, consider the two polyimides resulting from methylene dianiline-toughened bismaleimide (BMI–MDA) and diallylbisphenol-toughened bismaleimide (BMI–DAB). Both have a similar flexural modulus (0.5 and 0.53 msi, respectively), but BMI–DAB has over twice the flexural strength (25.5 vs. 10.9 ksi).[1]

More recently, polymer processing has begun to play an increasingly important role. The conditions under which the polymer is processed will dramatically affect the product material's final mechanical and chemical properties. Hence, the properties of a particular polymer can be tailored for a specific application. In the case of cyanate esters, stopping the reaction at 85% conversion will increase its density,

dielectric constant, Young's modulus, and solvent absorption relative to a complete cure.[2] However, a complete cure will result in an increase in hydrolytic stability and the glass transition temperature.[2] Since a thermoset involves an exothermic reaction, the rate at which the temperature is increased to the final cure temperature can play a significant role in determining the final properties of the product material. For thin components, or composites with a low mass loading of polymer, the temperature may be ramped more rapidly than for thick components where heat does not dissipate as rapidly. For these components, there is a greater likelihood of a runaway exotherm. Even in the absence of a runaway exotherm, temperature gradients within the component can lead to varying degrees of cure, causing internal stresses which can lead to future component failure. In addition to temperature, the autoclave pressure and atmosphere can have dramatic effects on the final properties. For these reasons, the temperature programs used in commercial autoclaves have become increasingly complex. This complexity has made it more difficult to model thermoset cures using traditional thermal methods such as DSC and TGA. Hence, commercial autoclaves often rely on a trial-and-error method in which various programs are attempted, followed by testing of the cured material's properties. This process is time-consuming

---

and expensive both in the short and long term since the selected program may not necessarily be the most cost-effective way (in terms of cure time or energy required) to produce the desired properties.

These concerns have stimulated much research in an effort to develop methods for monitoring the cure reaction in real-time.[3-28] Ultimately, such methods could lead to intelligent processing with real-time feedback control. Herein, we report the remote real-time simultaneous monitoring of the local temperature and degree of reaction of a high-performance thermoset polymer (AroCy L-10) using fiber-optic Raman spectroscopy.

EXPERIMENTAL

Chemicals and Sampling

For the *in situ* experiment, 10.0 g of monomer were mixed with 0.2 g of nonylphenol (Aldrich) and 0.005 g of $Cu(acetylacetonate)_2$ (Sigma Chemicals). The mixture was degassed and a portion immediately transferred into a rectangular glass cell ($2 \times 40 \times 100$ mm). The fiber-optic probe was inserted into the cell and approximately centered. The thermocouple wires (copper-constantan) were inserted adjacent to the probe. The sample cell was placed in a programmable convection oven and the fiber-optic and thermocouple wires were fed through an outlet port which was subsequently sealed with glass wool.

Fiber-Optic Raman Instrumentation

Raman excitation was achieved using all lines of a Spectra-Physics Argon ion laser to pump a Ti : sapphire laser which was tuned for 819 nm output. The 819 nm output was filtered using an angle tuned dielectric filter centered at 820 nm with a 4 nm fwhm band pass (Chroma Technologies, Inc.) before being launched into the proximal end of the excitation fiber using a 10X microscope objective (Newport). The laser exited the distal end of the excitation fiber, irradiating the sample. The distal end of a collinear collection fiber collected the Raman and Rayleigh scattered radiation. An $f/2$ lens was used to collimate the radiation exiting from the proximal end of the collection fiber. The Rayleigh scatter was then removed using a holographic supernotch filter centered at 819 nm (Kaiser Optical, Inc.). An $f/4$ lens was then used to focus the Raman-scattered radiation onto the slits of an image-corrected spectrograph (Chromex Model 250IS). The Raman-scattered radiation was dispersed using a 300 groove/mm grating

blazed at 0.9 microns. A Princeton Instruments UV-enhanced CCD detector (1152×298 pixels) was used to collect the Raman spectra. The fiber-optics were 200 μm core/220 μm cladding ultralow-OH silica fibers (Polymicro, Inc.).

In Situ Experiment

The total length of the *in situ* experiment was 420 min. During this time, 84 spectra were acquired: one 30-s acquisition every 5 min. Each spectrum included the anti-Stokes region from -900 to 0 cm^{-1} as well as the Stokes region from 0 to 2400 cm^{-1}.

The temperature program was modeled from one currently used in commercial autoclaves. The initial oven temperature was $20°C$. The oven temperature was ramped at $0.75°C/min$ for 120 min, held at $110°C$ for 60 min, ramped at $0.67°C/min$ for 60 min, held at $150°C$ for 60 min, ramped at $0.5°C/min$ for 60 min, and then held at $180°C$ for 60 min. Both oven temperature and thermocouple readouts were acquired periodically throughout the experiment. Prior to any spectral calculations, the spectral intensities for each spectrum were ratioed against the integrated area of the phenyl-ring stretch at 1599 cm^{-1}. Principal component analysis and regression was performed using Pirouette software (Infometrix).

RESULTS AND DISCUSSION

The structure of AroCy L-10 is shown in Scheme 1 along with the proposed reaction mechanism.[2] The reaction is catalyzed by a hydrogen donor (in this case, nonylphenol) and a metal chelating agent which facilitates the cyclization step. Once trimerization occurs, the pendant cyano groups can react further to form a highly crosslinked network.

Using the instrumental setup described above, the Raman spectra of AroCy L-10 were acquired in real-time as the oven temperature was controlled using the preprogrammed temperature ramp. The temperature program is one which is currently used in commercial autoclaves for the purpose of maximizing mechanical properties of the thermoset while avoiding runaway exotherms which introduce internal thermal stresses and possible chemical breakdown.[2] Three-dimensional plots of the acquired Stokes Raman spectra for the *in situ* experiment are shown in Figures 1 and 2.
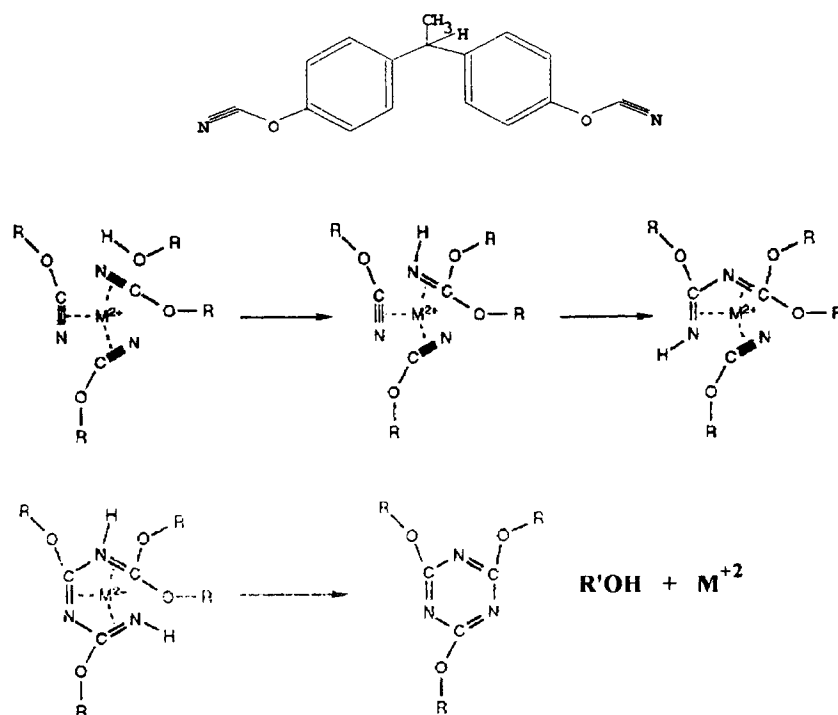
Scheme 1

Determination of Temperature

The Raman spectrum of AroCy L-10 both before and after thermal polymerization is shown in Figure 3. At zero-shift, it can be seen that the majority of the Rayleigh scatter from the laser is removed by the holographic notch filter. This enables both the Stokes and anti-Stokes Raman-scattered radiation to be collected in a single acquisition. For AroCy L-10, there is a relatively intense mode at 633 cm^{-1} (a CH out-of-plane deformation of a phenyl ring) which is resolved and does not undergo significant change during the polymerization reaction. Due to its low energy, this mode also exhibits a relatively intense anti-Stokes peak at −633 cm^{-1}. Since the anti-Stokes scatter results from excitation of molecules which are in a vibrationally excited state, the intensity of this mode is dependent not only on the Raman cross section, but also on the temperature of the sample. The Stokes-scattered radiation results from excitation of molecules which are in the vibrational ground state. Hence, there is no temperature dependence for the Stokes intensity. Since both Stokes and anti-Stokes Raman peaks originate from the same mode, the Raman cross sections are identical. Thus, a ratio of the anti-Stokes and Stokes peaks should give a Boltzmann relationship with respect to temperature. Since the efficiency of the Raman scattering process is inversely proportional

to λ,^{4} where λ is the wavelength of scattered radiation, a correction for the differences in the Stokes and anti-Stokes wavelengths must be used. An additional correction term must be used since the silicon detector has a different quantum efficiency (and the spectrograph and fiber probe have different optical efficiencies) for the Stokes and anti-Stokes photons. The complete relationship is given in eq. (1):

$$\frac{I_{as}}{I_s} = \frac{\lambda_s^4}{\lambda_{as}^4} \times \frac{\Phi_{as}}{\Phi_s} \times \exp \frac{-\Delta E}{kT} \qquad (1)$$

where ΔE is the vibrational energy of the 633 cm^{-1} mode (1.26×10^{-20} J); k, the Boltzmann constant (1.38×10^{-23} J/K); and T, the temperature in degrees Kelvin. Rearrangement of eq. (1) yields a linear relationship:

$$\ln \frac{I_{as}}{I_s} = \frac{-\Delta E}{k} \frac{1}{T} + C \qquad (2)$$

where the constant C incorporates corrections for the wavelength dependence of the instrument and the wavelength dependence of the scattering process. The value of C can be empirically determined prior to the experiment by constructing a linear calibration curve ($\ln I_{as}/I_s$ vs. T^{-1}) using the fully cured
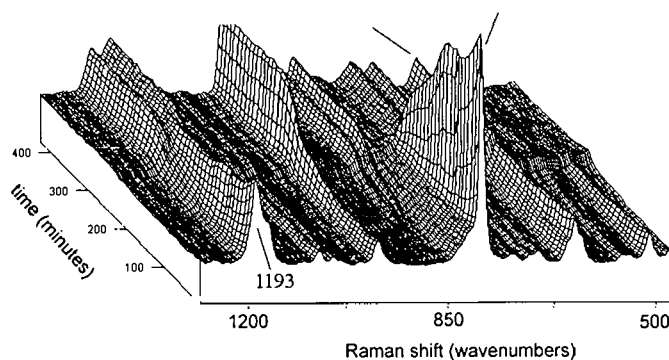
Figure 1 Stokes Raman spectra of fingerprint region of AroCy L-10. Spectra were taken in real-time during the thermal cure of the polymer within an oven. Although 84 spectra were acquired (one 30-s spectrum every 5 min), only 42 are displayed (one every 10 min) for spectral clarity.

polymer at several known temperatures. Once C has been determined, the ratio of intensities can be used to determine the temperature of the sample in real-time during subsequent experiments.

For the *in situ* experiment, the ln I_{as}/I_s was plotted against the reciprocal temperature for the oven program (Fig. 4). A linear relationship is observed as suggested by eq. (2). In addition, using eq. (2), the temperatures were calculated from spectra taken 10 min apart (30 s spectra were acquired every 5 min) and plotted vs. experimental time (Fig. 5). Figure 5 also contains a plot of the temperature determined from a thermocouple embedded in the center of the sample adjacent to the fiber-optic probe tip, as well as the programmed oven temperature. It is worth noting that both the thermocouple and the fiber-optic probe yield "local" sample temperatures, while the oven temperature refers to the air temperature within the oven. As shown in Figure 5, the thermocouple data and the fiber-optic Raman data yield similar results. Note that both of the "local" temperatures show a departure from the oven temperature during the first 50 min of the cure cycle. This local temperature increase is likely due to slow heat dissipation within the sample as the exothermic reaction is initiated. Note that this same deviation with respect to local and oven temperatures is observed in Figure 4, explaining the slight departure from linearity at the plot extreme.

After the first 225 min of cure, there is an increase in the scatter of the Raman-determined temperatures, although the general trend still follows that of the thermocouple data. As will be shown, this increased error is due to spectral changes caused by vitrification of the sample as the cure proceeds.

Univariate Determination of Percent Cure

As shown in Figures 1 and 2, there are several significant changes in the Raman spectrum of AroCy as the cure proceeds. Two distinct peaks at 801 and 1193 cm^{-1} in the uncured spectrum of AroCy are due to the cyano–ether linkage deformation and stretch. Upon reaction, the peak at 801 cm^{-1} shifts to higher energy (854 cm^{-1}) due to branching at the alpha carbon (the first step in the cyclization reaction shown in Scheme 1). This new mode at 854 cm^{-1} has both low- and high-energy shoulders. The 1193 cm^{-1} ether linkage mode is also split into two modes (1172 and 1203 cm^{-1}). Accordingly, this splitting arises from branching at the carbon atom adjacent to the oxygen atom. In the uncured sample, two relatively weak peaks are seen at 2239 and 2267 cm^{-1}. These peaks arise from the symmetric and asymmetric CN modes. As the cure reaction proceeds, both these intensities decrease to zero. Although these modes appear weak in the spectra, their Raman cross section is actually higher than that of the strong mode at 1193 cm^{-1}. The low spectral intensity is due to a decrease in detector sensitivity at the longer wavelengths. Indeed, for this same reason, the CH stretching region cannot be detected with the present detector. At 986 cm^{-1}, an intense peak grows in during the cure reaction due to the symmetric triazine ring breathing mode. As shown in Scheme 1, the triazine ring is formed in the final cyclization step of the reaction.

In addition to the above-mentioned spectral changes which are indicative of the underlying chemistry of the system, there are several modes whose energies and Raman cross sections remain
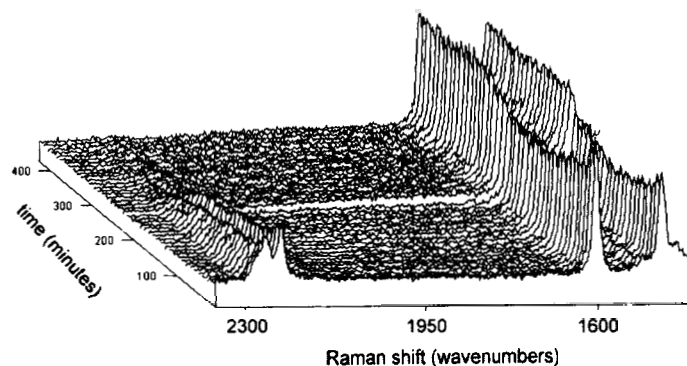
Figure 2   Stokes Raman spectra of CN and phenyl stretching region of AroCy L-10. Spectra were taken in real-time during the thermal cure of the polymer within an oven. Although 84 spectra were acquired (one 30-s spectrum every 5 min), only 42 are displayed (one every 10 min) for spectral clarity.

unvaried throughout the experiment. These include the 633 cm^{-1} peak discussed previously, as well as the phenyl ring stretching modes at 1455 and 1599 cm^{-1}. These modes are analytically useful since they can serve as internal standards to correct for fluctuations in laser power and changes in sample refractive index (resulting in changes in fiber collection efficiency) and sample density as the reaction proceeds. For this reason, the spectral intensities for each spectrum were ratioed against the integrated intensity of the peak at 1599 cm^{-1} prior to any calculations. The need for an internal standard can be seen by viewing Figure 2. As the reaction time exceeds 200 min, there is a drop of in the CN intensity. Concomitant with this is a sudden increase in the intensity of the phenyl modes at 1599 and 1450 cm^{-1}. This is due to vitrification of the AroCy (originally present as a viscous liquid) and a resulting change in the sample's refractive index and density.

Inspection of the above spectral changes suggests several possibilities for quantitating the extent of
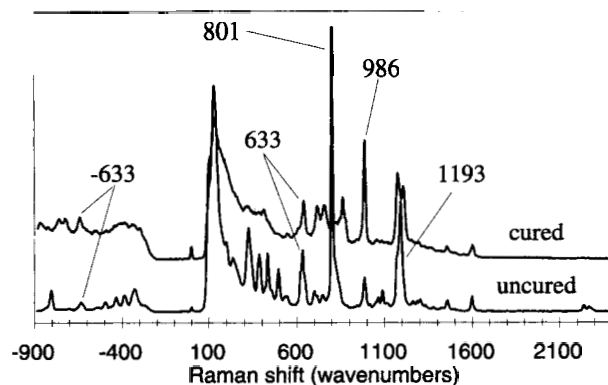
reaction. The most dramatic change is the decrease in intensity of the 801 cm^{-1} mode. However, even after complete reaction, there is still some spectral intensity present at 801 cm^{-1} due to the low-energy shoulder on the new mode which grows in at 854 cm^{-1}. A second possibility is the ring-breathing mode which grows in at 986 cm^{-1}. However, prior to the appearance of this mode, there is already a weak peak at 990 cm^{-1} in the unreacted sample. The only spectral region which shows a significant spectral change in the absence of interfering peaks is the CN stretching region above 2200 cm^{-1}. Unfortunately, these peaks are relatively weak, resulting in a low signal-to-noise ratio. The prediction of % cure using each of these three regions is shown in Figures 6–8. For the two regions where the integrated spectral intensity decreases as the reaction proceeds, the %
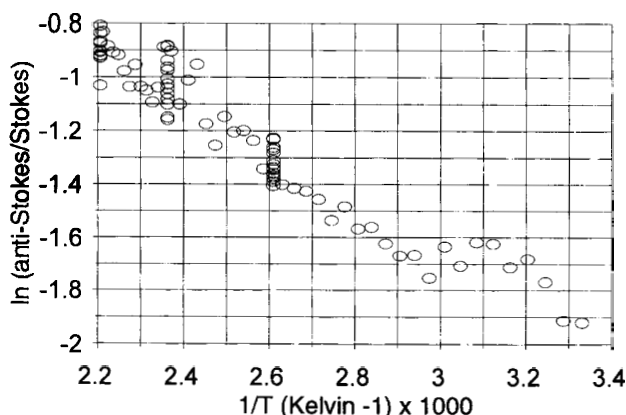

Figure 3   Stokes and anti-Stokes Raman spectra for AroCy L-10 both before and after thermal cure.

Figure 4   Correlation of the anti-Stokes-to-Stokes intensity ratio for the 633 cm^{-1} mode of the *in situ* spectra to the reciprocal oven temperature. The deviation from linearity at low temperatures is due to a difference in the "local" sample temperature and the oven temperature.
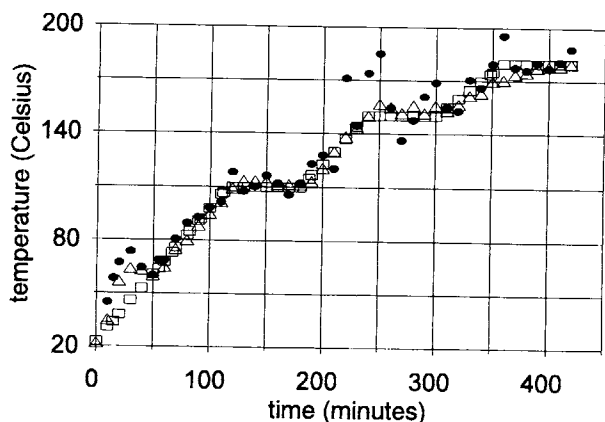
Figure 5 Plot of temperatures as a function of time for the *in situ* experiment. Solid circles represent temperatures determined from Raman data, triangles represent temperatures determined from thermocouple data, and squares correspond to the oven temperature. The Raman and thermocouple data corresponds to "local" sample temperatures.

cure was calculated using the following relationship for the normalized spectra:

$$\% \ CURE = \left[1 - \frac{I_x - I_\alpha}{I_0}\right] \times 100\% \qquad (3)$$

where I_x is the integrated intensity for the desired spectral region and the subscript refers to the spectral acquisition time (e.g., $t = 0$ for uncured, $t = \infty$ for completely cured, $t = x$ for cure after x min have elapsed). In the case where a peak is growing in, the relationship is defined as follows:
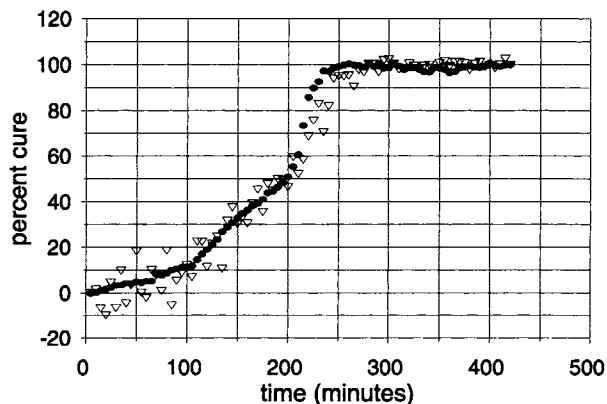

Figure 6 Plot of percent cure as a function of cure time for the *in situ* experiment. Triangles correspond to the percent cure determined using the integrated CN stretching region. Solid circles correspond to the percent cure determined using principal components regression.
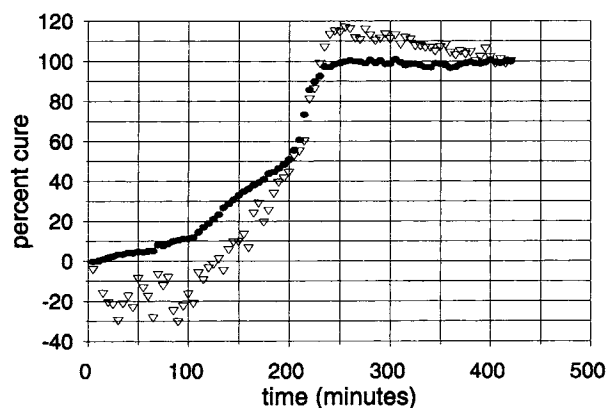

Figure 7 Plot of percent cure as a function of cure time for the *in situ* experiment. Triangles correspond to the percent cure determined using the integrated 801 cm⁻¹ peak. Solid circles correspond to the percent cure determined using principal components regression.

$$\% \ CURE = \left[\frac{I_x - I_0}{I_\alpha}\right] \times 100\% \qquad (4)$$

Use of either eq. (3) or (4) requires that the spectrum of both a cured and an uncured sample be acquired prior to the *in situ* experiment (using the same experimental setup) if the % cure determinations are to be performed in real-time.

The calculated % cure using the CN stretching modes is plotted (triangles) in Figure 6. Of the three spectral regions, this region is expected to give the most straightforward correlation between degree of cure and intensity since this is the only region without interfering peaks. During the initial ramp of the program, a slight decrease in the CN intensity in-
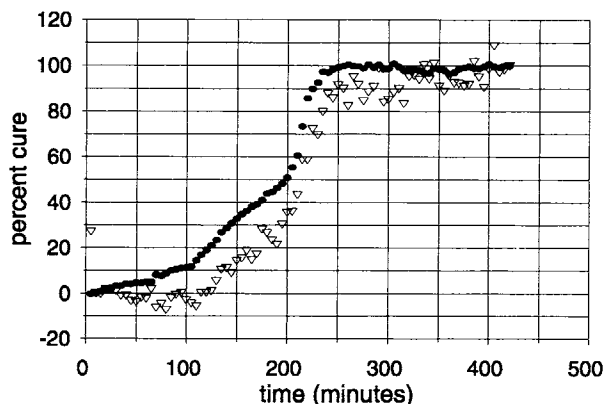

Figure 8 Plot of percent cure as a function of cure time for the *in situ* experiment. Triangles correspond to the percent cure determined using the integrated area of the 986 cm⁻¹ peak. Solid circles correspond to the percent cure determined using principal components regression.

dicates a slow rate of cure. Once the isothermal portion of the program is reached (110°C), the rate of reaction begins to accelerate. By going isothermal as the reaction rate increases, the likelihood of a runaway exotherm is minimized. When the temperature is increased to 150°C, the rate of reaction accelerates dramatically until it reaches 100% cure at < 300 min (CN intensity is no longer evident).

In the case of the decreasing ether linkage mode at 801 cm^{-1} (triangles plotted in Fig. 7), the resulting % cure plot is more complicated. Initially, the integrated intensity is observed to increase, resulting in an apparent decrease in the % cure. As seen with the CN region, inflections in the cure curve are also observed at the 120 min mark as well as the 200 min mark. Surprisingly, by the 250 min mark, the calculated % cure exceeds 110% before dropping back to 100% at the 420 min mark. The impossibility of negative % cure as well as the impossibility of greater than 100% cure suggests the presence of an interfering peak(s) which grows in as the ether linkage decays to zero.

The % cure as determined by the growth of the triazine mode is plotted as triangles in Figure 8. During the first 100 min of the experiment, no change in integrated intensity is observed in this region. At the 120 min mark, the reaction begins to proceed at a rate which is similar to that of the CN plot (i.e., same slope). As in the CN plot, the rate increases at the 200 min mark before leveling off between 250 and 300 min with a percent cure of 90%. Although there is a greater degree of scatter in the final 200 min of the experiment, it appears that the reaction is completed (100% cure) after the 300 min mark.

When comparing the different spectral regions, several conflicting trends can be observed. For example, due to spectral complexities, a decrease in % cure, an increase in % cure, and no change in % cure are observed for the respective plots during the first 100 min of the cure. For this reason, we attempted a multivariate determination of the % cure.

Multivariate Determination of Percent Cure

In recent years, principal component analysis (PCA) and principal component regression (PCR) methods have been used to solve a wide variety of chemical problems which require the use of multivariate analysis. The first step involves decomposition of a row matrix (X) containing the input spectra into a loading matrix (L) and a score matrix (S) so that the product of these two matrices yields the original input spectra:

$$X = S \times L \qquad (5)$$

$$\begin{pmatrix} I^a_{\lambda_1} & I^a_{\lambda_2} & \cdot & \cdot \\ I^b_{\lambda_1} & I^b_{\lambda_2} & \cdot & \cdot \\ \cdot & \cdot & & \\ \cdot & \cdot & & \end{pmatrix}$$

$$= \begin{pmatrix} S^{PC}_{a}1 & S^{PC}_{a}2 & \cdot & \cdot \\ S^{PC}_{b}1 & S^{PC}_{b}2 & \cdot & \cdot \\ \cdot & \cdot & & \\ \cdot & \cdot & & \end{pmatrix} \begin{pmatrix} L^{PC}_{\lambda_1}1 & L^{PC}_{\lambda_2}1 & \cdot & \cdot \\ L^{PC}_{\lambda_1}2 & L^{PC}_{\lambda_2}2 & \cdot & \cdot \\ \cdot & \cdot & & \\ \cdot & \cdot & & \end{pmatrix}$$

Here, the sub- and superscripts "a" and "b" refer to two different spectra. In matrix X, each spectrum is defined by intensities (I) at given wavelengths (or wavenumbers). Each row vector in the loading matrix is referred to as a principal component and consists of a single loading value (L) for each spectral wavelength. Hence, the first-row vector in the loading matrix above would correspond to principal component 1 (PC$_1$), the second row to PC$_2$, and so on. The magnitude of a particular loading (for a given principal component) indicates how much information that wavelength contributes to the principal component. The maximum number of possible principal components is equal to the number of wavelengths in the spectrum or one less than the number of spectra in matrix X. The scores matrix simply relates the principal components back to the original spectra, i.e., the scores define how much a particular principal component contributes to a spectrum. Thus, the first row vector of the scores matrix tells how much PC$_1$ and PC$_2$ (etc.) contribute to spectrum "a." Alternatively, the first column vector in the scores matrix indicates how much PC$_1$ contributes to each spectrum in the X matrix.

The principal components are ranked in order of variance, i.e., PC$_1$ accounts for the greatest amount of variance in the set of input spectra. For this reason, the vast majority of the spectral information is included in the first few principal components, while the higher principal components are composed mostly of noise. Often, the chemical information contained in the input spectra can be easily interpreted by viewing the first few principal components. It is for these two reasons that performing a principal component regression is preferred to directly regressing the spectral wavelengths (i.e., a multiple linear regression).

To better understand the reaction chemistry of the in situ experiment, a principal component analysis was performed using all of the in situ spectra to construct matrix X and then decomposing it into the loadings and scores matrices. In the absence of mean-centering, the first principal component gen-

erally mirrors the mean of the input spectra, and, hence, little information as to the reaction chemistry is provided.[29] The second principal component, however, provides a great deal of information. The loadings for PC_2 are plotted as a thin line in Figure 9. The loadings indicate that curing of the sample results in a decrease in the peak at 801 cm^{-1} (the ether linkage deformation), as well as an increase in spectral intensity on the high- and low-energy side of the 801 cm^{-1} peak. This is consistent with the *in situ* spectra shown in Figure 1 and accounts for the anomalies noted above for the 801 cm^{-1} % cure plot (Fig. 7). There is an increase in spectral intensity at 986 cm^{-1}, consistent with the new triazine mode. For the uncured AroCy spectrum, this region shows a peak at 990 cm^{-1}, suggesting that more than one mode is present. At 1193 cm^{-1}, there is a decrease in intensity, concurrent with an increase in intensity on both the high- and low-energy shoulders. This is consistent with the splitting of the ether-linkage stretch observed in Figure 3. There are decreases in intensity at both 2267 and 2239 cm^{-1}, consistent with the disappearance of the CN modes as the reaction proceeds. It is worth noting that the phenyl stretching modes at 1455 and 1599 cm^{-1} have loadings which are effectively zero. This indicates that these modes are not appreciably affected by the cure reaction. Thus, PCA readily identifies the spectral changes which occur during the cure reaction.

The scores column vector for PC_2 is shown in Figure 10 (right-hand axis). This plot indicates how

Figure 10 Plot of the principle component 2 scores (triangles with line) for each *in situ* spectra (each spectrum taken at a unique time). These scores were determined after the completion of the *in situ* experiment. Plot of the predicted percent cure (open circles) determined in real-time for the *in situ* experiment using the PCR calibration.
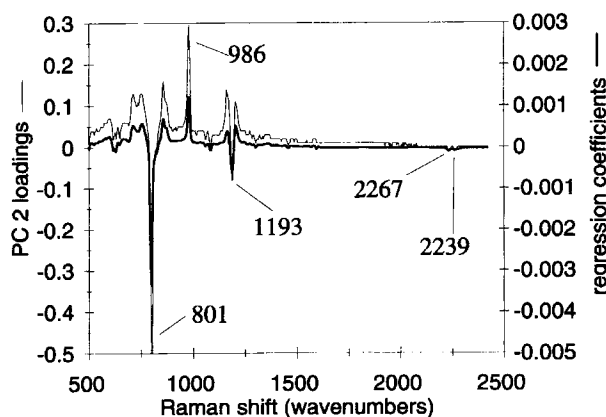
Figure 9 Plot of the loadings for principal component 2 as a function of Raman Stokes shift (thin line). The loadings were determined by performing a PCA on the *in situ* spectra after the experiment had concluded. Plot of the regression coefficients (thick line) determined by performing PCR on cured and uncured spectra prior to commencing the *in situ* experiment.
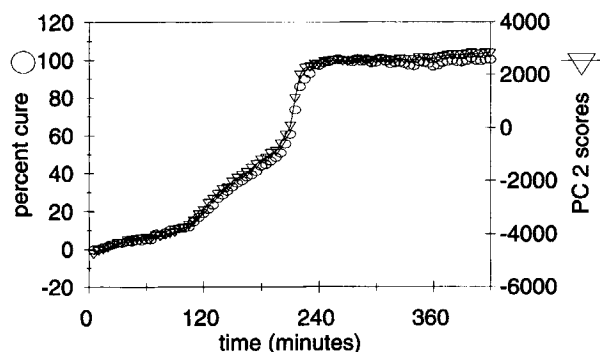
much PC_2 contributes to each spectrum (acquired at a specific time during the cure program). During the initial stages of the cure, the scores are low, but as the reaction proceeds, the scores increase. Indeed, the shape of the scores plot matches well with the % cure plot obtained from the univariate analysis of the CN stretching region (Fig. 6). Since the loadings of PC_2 are consistent with spectral changes which occur upon cure of the sample, it follows that the score for PC_2 should increase for spectra which are taken after longer times of reaction.

To determine the % cure in real-time using principal component regression analysis, two spectra were acquired both before the temperature program was initiated and after the temperature program was completed. These four spectra were then used to construct matrix **X**, which was subsequently decomposed (using singular value decomposition). A matrix (**Y**) of the % cures for the four spectra was constructed using 0% percent cure for the first two spectra and 100% cure for the final two spectra. Since **Y** and **X** are known for this calibration, the regression coefficients (*B*) can be solved for. The regression coefficient matrix **B** is a single-column vector with each coefficient corresponding to a particular wavelength. The % cure for any spectrum is the scalar value, resulting from the product of that spectrum (row vector) and the column vector of regression coefficients. The regression coefficients are plotted in Figure 9 (thick line), and the resulting predicted % cure for each spectrum is plotted in Figure 10 (open circles).

It is reassuring to note that the regression coefficients match almost exactly the loadings for PC_2. This indicates that the regression resulting from

uncured and fully cured spectra describes the full chemistry of the cure cycle. It also indicates, as we suggested above, that PC_2 describes the cure chemistry, and little contributions are made by the other principal components. Any slight differences in the loadings and the regression coefficients are due to either small contributions from additional PCs (with respect to the regression coefficients) or, alternatively, small contributions to the loadings due to intermediate chemical species formed during the reaction. Regardless, neither appears to be significant.

It is also reassuring that the predicted % cure (based on the uncured and fully cured spectra) overlays the PC_2 scores based on the full *in situ* cure (Fig. 10). Unlike the univariate predictions of % cure, this method utilizes all of the available spectral information. Indeed, it can be seen (overlaid plots in Figs. 6–8) that of all the % cure plots the multivariate plot has the least scatter. Significantly, the multivariate predictions show a much closer resemblance to the CN-based predictions than to that of the triazine and the ether linkage-based predictions despite the fact that the CN region shows minimal loadings when compared to the rest of the spectrum. The closer resemblance of the multivariate predictions to the CN predictions confirms the spectral interferences for the predictions based solely on either the ether-linkage mode or the triazine mode. It is noteworthy that the multivariate regression contains the information included in the 1193 cm^{-1} region since it is not possible to use this region for univariate predictions.

The % cure predicted from the multivariate model is overlaid with the temperature program in Figure 11. There are four distinct regions of the % cure plot (A, B, C, and D). During the first stage of the cure (A), the rate of cure is gradual. Just as the rate begins to increase in the transition from A to B, the temperature program goes isothermal. Even though the program remains isothermal, the reaction continues to accelerate in region B. It is logical to assume that the reason behind the isothermal leg of the ramp is to prevent the reaction from running away. Toward the end of region B, the reaction rate begins to decrease slightly, and in response, the temperature program begins a new thermal ramp. This results in a renewed increase in the reaction rate until 100% cure is reached. The point of 100% cure coincides with the second isothermal leg of the temperature program. The last two legs of the temperature program appear to have no effect on the % cure. It is possible that these last two legs could be eliminated and thus reduce cure time and expense. Alternatively, these last two legs may involve a desired an-
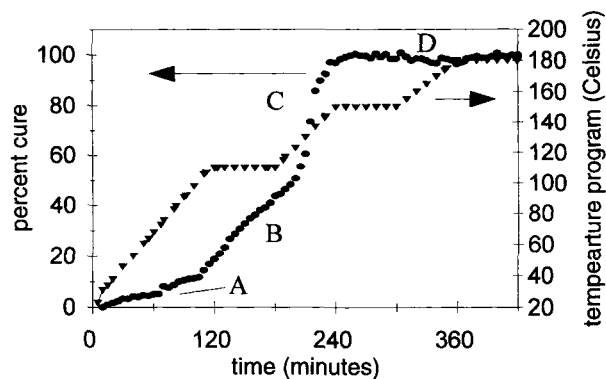

Figure 11 Overlay plot of the real-time predicted percent cure using PCR (circles) and the oven temperature program (triangles). Four distinct regions of the cure plot are marked as A, B, C, and D.

nealing process to further modify the thermoset. In this case, the % cure plot indicates that the annealing steps could be initiated up to 50 min earlier in the program. Regardless, it is clearly evident that real-time *in situ* feedback from the fiber-optic Raman probe can facilitate the development of efficient thermal cure programs.

The multivariate models were carried out on both the normalized spectra as well as the raw spectra. Both treatments yield identical results, suggesting that a resolved internal reference peak is not required for this system to obtain valid quantitative results when using multivariate calibration. This is consistent with other quantitative Raman investigations using multivariate analysis.[30,31]

CONCLUSIONS

Fiber-optic Raman spectroscopy allows both the local temperature of the polymer and its reaction chemistry to be monitored in real-time. The local temperature of the sample determined using both the Raman Stokes and anti-Stokes scattering of a reference peak correlates well with the local temperature determined using a thermocouple probe. The reaction chemistry can be monitored in real-time using both univariate and multivariate methods. The use of principal component regression analysis in monitoring the reaction chemistry offers several advantages over univariate methods: (1) spectral interference associated with univariate methods is eliminated; (2) all available spectral information can be used in the regression resulting in more accurate predictions; (3) the principal component regression based solely on uncured and fully

cured spectra can be validated after the experiment by performing a principal component analysis on the *in situ* spectra; and (4) a resolved internal reference peak is not required. The use of principal component analysis is also helpful in elucidating the spectral changes which take place during the cure cycle (i.e., the reaction chemistry) and in identifying spectral features which are invariant of the cure chemistry.

It has been demonstrated that fiber-optic Raman spectroscopy provides a facile means of monitoring thermoset reactions in real-time. The ability to monitor the local sample temperature allows heat buildup to be identified before runaway exotherms can occur. This information coupled with the real-time changes in the sample's chemistry could be used in a feedback loop for the temperature controller. In this regard, the technique should provide a feasible base for an intelligent processing control system.

REFERENCES

1. M. Bargain, U.S. Pat. 3,562,223 (1971); S. P. Qureshi, U. S. 4,774,282 (1988).

2. D. A. Shimp, J. R. Christenson, and S. J. Ising, *AroCy Cyanate Ester Resins: Chemistry, Properties and Applications;* 2nd ed., Rhone-Poulenc, Louisville, KY, 1990.

3. S. S. Saliba, T. E. Saliba, and J. F. Lanzafame, *Int. SAMPE Symp. Exhib. (Tomorrow's Mater.: Today, Book 1),* **34,** 397–406 (1989).

4. D. E. Kranbuehl, P. Kingsley, S. Hart, A. Loos, G. Hasko, and B. Dexter, *SAMPE Symp.,* **37,** 907–911 (1992).

5. D. A. C. Compton, S. L. Hill, N. A. Wright, M. A. Druy, J. Piche, W. A. Stevenson, and D. W. Vidrine, *Appl. Spectrosc.,* **42**(6), 972–979 (1988).

6. D. E. Kranbuehl, *Polym. Prepr.,* **31**(1), 289–290 (1990).

7. D. E. Kranbuehl, T. J. Kim, S. C. Liptak, and J. E. McGrath, *Polym. Prepr.,* **34**(2), 488–489 (1993).

8. D. E. Kranbuehl, in *Encyclopedia of Composites,* S. Lee, Ed., VCH Publishers, New York, 1989, pp. 531–543.

9. J. M. Cartwright, S. A. Srinivasan, J. E. McGrath, A. C. Loos, T. C. Ward, D. Hood, and D. E. Kranbeuhl, in *Adhesion Society, Proceedings of the Seventeenth Annual Meeting Symposium Part. Adhesion,* 1993,

K. M. Liechti, Ed., Adhesion Society, Austin, TX, 1994, pp. 62–65.

10. G. Prokopowicz, H. J. Paik, F. Wong, and N. Sung, *Polym. Mater. Sci. Eng.,* **71,** 347–348 (1994).

11. J. Mijovic and S. Andjelic, *Polymer,* **36**(19), 3783–3786 (1995).

12. E. W. Nelson and A. B. Scranton, *Polym. Mater. Sci. Eng.,* **72,** 413–414 (1995).

13. G. R. Powell, P. A. Crosby, G. F. Fernando, C. M. France, R. C. Spooncer, and D. N. Waters, *Proc. SPIE-Int. Soc. Opt. Eng.,* **2444,** 386–395 (1995).

14. T. G. Kotch, A. J. Lees, S. J. Fuerniss, and K. I. Papathomas, *Chem. Mater.,* **7**(4), 801–805 (1995).

15. Z. Ge, C. W. Brown, and M. Brown, *J. Appl. Polym. Sci.,* **56**(6), 667–775 (1995).

16. J. F. Maguire and P. L. Talley, *J. Adv. Mater.,* **26**(2), 27–40 (1995).

17. T. E. Saliba, D. Hofmann, and P. Smolinski, *Compos. Sci. Technol.,* **51**(1), 1–9 (1994).

18. E. E. Tapanes, A. J. Hill, and P. L. Rossiter, in *Proceedings of the 9th International Conference on Composite Materials,* A. Miravete, Ed., University of Zaragoza, Zaragoza, Spain, 1993, Vol. 2, pp. 457–464.

19. R. E. Lyon, K. E. Chike, and S. M. Angel, *J. Appl. Polym. Sci.,* **53**(13), 1805–1812 (1994).

20. J. M. Fildes, S. M. Milkovich, R. Altkorn, R. Haidle, and J. Neatrour, *Int. SAMPE Tech. Conf. (Adv. Mater.: Expanding the Horizons),* **25,** 887–900 (1993).

21. L. Xu, J. H. Fu, and J. R. Schlup, *J. Am. Chem. Soc.,* **116**(7), 2821–2826 (1994).

22. T. Saliba, S. Saliba, J. Lanzafame, and L. Gudeman, *Int. SAMPE Symp. Exhib. (Mater. Work. You 21st Century),* **37,** 1445–1454 (1992).

23. T. M. Stokich, Jr., W. M. Lee, and R. A. Peters, *Mater. Res. Soc. Symp. Proc. (Mater. Sci. High Temp. Polym. Microelect.),* **227,** 103–114 (1991).

24. M. A. Druy, P. J. Glatkowski, and W. A. Stevenson, *Proc. SPIE-Int. Soc. Opt. Eng. (Fiber Opt. Laser Sens. 9),* **1584,** 48–52 (1991).

25. J. R. Walton and K. P. J. Williams, *Vib. Spectrosc.,* **1**(4), 339–345 (1991).

26. B. Z. Jang, H. B. Hsieh, and M. D. Shelby, *Polym. Compos.,* **12**(1), 66–74 (1991).

27. A. Udagawa, F. Sakurai, and T. Takahashi, *J. Appl. Polym. Sci.,* **42**(7), 1861–1867 (1991).

28. G. A. George, P. Cole-Clarke, N. St. John, and G. Friend, *J. Appl. Polym. Sci.,* **42**(3), 643–657 (1991).

29. R. A. Johnson and D. W. Wichern, *Applied Multivariate Statistical Analysis,* 3rd ed., Prentice Hall, Englewood Cliffs, NJ, 1992, Chap. 8.

30. J. B. Cooper, P. E. Flecher, T. M. Vess, and W. T. Welch, *Appl. Spectrosc.,* **49**(5), 586–592 (1995).

31. J. B. Cooper, K. L. Wise, J. Groves, and W. T. Welch, *Anal. Chem.,* **67**(22), 4096–4100 (1995).